

Skyrmionic SU(6) structured light

Shinichi Saito

Center for Exploratory Research Laboratory, Research & Development Group, Hitachi, Ltd. Tokyo 185-8601, Japan.
shinichi.saito.qt@hitachi.com

ABSTRACT

Skyrmions are topological quasi-particles characterised by local spin textures, which are considered to be robust against structural deformation. Néel and Bloch states are famous examples of skyrmions, which exhibit radical and chiral spin profiles, respectively. Here, we show a skyrmion can be continuously transformed to an antiskyrmion or various other forms of skyrmions through underlying symmetry of special unitary group of degree six, SU(6), for photons with spin and orbital angular momentum. We employ a Lie group theory for coherent photons to describe the SU(6) transformation and establish a relationship between the generator of rotation and its expectation values on a hypersphere of \mathbb{S}^{35} . We propose a simple experimental setup to control the SU(6) states in combinations with wave-plates and vortex lenses to realise the generalised Euler's formula physically in a Mach-Zehnder interferometer. We show skyrmionic states are described on higher-order Poincaré spheres together with a recently proposed skyrmionic torus.

Introduction

The elementary particle physicist, Tony Skyrme, proposed to solve the mechanism why nucleons such as protons and neutrons are so stable in quantum chromodynamics (QCD) by introducing the concept of the topological invariance¹. He employed a model Lagrangian to describe interacting meson fields and obtained a classical solution, whose spin texture is characterised by a whirl of spin like a hedgehog, pointing along the radial direction over three-dimensional space (\mathbb{R}^3)¹. Skyrme conjugated the winding number in the homotopy mapping from three-sphere (\mathbb{S}^3) to \mathbb{S}^3 , described as $\pi_3(\mathbb{S}^3) = \mathbb{Z}$, where \mathbb{Z} is the set for all integers, corresponds to the baryon number, B , and considered baryons are solitons in the non-linear sigma model². The innovative idea of generating a fermion out of bosons could not attract significant attentions in 1960s, and it took two decades to achieve the canonical quantisation of the topological soliton^{3,4}, which is named a skyrmion⁵. Witten theoretically introduced the N colour charges and developed the theory of the special unitary group, SU(N), in the limit of $N \rightarrow \infty$ ⁶, where QCD is equivalent to an effective theory of mesons³. Remarkably, it was proved that the classical solution of Skyrme becomes exact in this limit⁶ and the quantum fluctuation is suppressed as the higher order effect in $1/N$ expansion, showing a skyrmion is a fermion if N is odd^{3,4}. In reality, the number of colour charges is three in QCD, and thus, a skyrmion is indeed quantised as a fermion^{3,4}. In a modern perspective, however, the standard model describes hadrons based on quarks⁷⁻⁹ and SU(6) symmetry^{10,11} of a vacuum without introducing skyrmions, which were not discovered as elementary particles unlike quarks. Consequently, the relationship between a skyrmion¹⁻⁶ and SU(6) symmetry⁷⁻⁹ has not been completely established, yet.

Regardless of the absence of a skyrmion in original high-energy elementary particle physics, various forms of skyrmions were successfully discovered in low-energy condensed-matter physics as quasi-particles in magnets¹²⁻¹⁹, quantum Hall systems²⁰, superconductors^{21,22}, liquid crystals²³, Bose-Einstein condensates²⁴, and photonic systems²⁵⁻³⁸. In these systems, skyrmions are also known as baby skyrmions^{13,39}, since they are realised in two-dimensional space (\mathbb{R}^2), whose spin texture can be mapped onto the surface of two-sphere (\mathbb{S}^2) by a stereographic projection^{17-19,36,40}, corresponding to the homotopy mapping of $\pi_2(\mathbb{S}^2) = \mathbb{Z}$. The integer to characterise topology of skyrmions is a skyrmion number, s , which is the number of times for spin to wrap over \mathbb{S}^2 ^{17,19,36}, and the higher order excitation is called a hopfion^{21,23,41-50}, since the map is related to the Hopf fibration^{40,51,52}. The simplest Hopf map^{40,51,52} is mathematically defined as a map from \mathbb{S}^3 to \mathbb{S}^2 , $\pi_3(\mathbb{S}^2) = \mathbb{Z}$, and the two-level quantum system of spin 1/2 is an excellent physical realisation of the Hopf map. In fact, the SU(2) wavefunction⁵² is described by two complex numbers (\mathbb{C}^2), which is normalised to be shown on \mathbb{S}^3 with a unit radius, and the wavefunction is mapped to give expectation values of spin, which is shown on \mathbb{S}^2 , known as the Bloch sphere⁵³. It is well-known that the gauge transformation in the global U(1) phase of the wavefunction preserves the spin expectation values, and the trajectory of the wavefunction upon changing the U(1) phase forms a great circle (\mathbb{S}^1) on \mathbb{S}^3 , which is mathematically known as a fibre^{40,51,52}. Each fibre shown as a circle represents a genuine state with unique expectation values associated with the state, and thus, the circles to give different expectation values will never cross each other, forming Villarceau circles and Clifford parallels upon the Hopf fibration^{40,51,52}. By mapping \mathbb{R}^2 to fibres of wavefunctions, skyrmions were observed^{12-20,23-38}, while hopfions were observed^{21,23,41-50} by including the U(1) phase into the map from \mathbb{R}^3 . For both skyrmions and hopfions, the Hopf map revealed the topological significance in spin textures to cover the entire Bloch sphere^{17,19,36,40,51,52}, and the Hopf

map is the correspondence^{17,19,36,40,51,52} between quantum mechanical wavefunction, represented by \mathbb{C}^2 , and the classical spin expectation values as observables, represented by \mathbb{R}^3 . The Hopf map^{17,19,36,40,51,52} suggests topological structures are indispensable to understand the crossover from quantum to classical behaviours^{10,54–56}.

The topological nature of quantum mechanics is already found in the crossover from Ising spin to Heisenberg spin^{53,57–59}. Ising spin is defined for a classical two-level system, characterised by zero-dimensional sphere, $\mathbb{S}^0 = \{1, -1\}$, which is isomorphic to the cyclic group of order two, $\mathbb{Z}_2 = \{0, 1\}$, and a basis of classical computing as a bit for gate logic. On the other hand, Heisenberg spin is defined for a quantum two-level system, characterised by \mathbb{S}^2 , which is a basis of quantum computing as a qubit⁶⁰. Based on the superposition principle, we can construct a unitary transformation from the spin-up state to the orthogonal spin-down state, whose continuous path can be drawn on \mathbb{S}^2 , such that a sphere in the higher dimension is a topological structure to show the crossover from classical to quantum states^{53,57–60}. Mathematically, this quantum-classical crossover is understood by the extension from \mathbb{Z}_2 to $SU(2)$ for describing a state. The topological signature of polarisation in light^{57–59,61} was also found in a polarisation ellipse, showing the locus and dynamics of the phase front depending on left and right circularly polarised states and their superposition, which is also described by $SU(2)$ symmetry shown on the Poincaré sphere of \mathbb{S}^2 . An important lesson to learn from this primitive example is that we can realise the topological transformation among classically distinguishable states by allowing a quantum superposition state between them in higher dimensions.

Topology and underlying symmetry are also important for structured light, which is characterised by an optical vortex with orbital angular momentum (OAM)^{62–78}. An optical vortex possesses topological charge (m), which is a winding number for an optical mode with an azimuthal (ϕ) dependence of the phase as $e^{im\phi}$ around the node^{62–78}. OAM is coming from rotational symmetry of the Laguerre-Gauss mode^{62,63}, which is described by the simplest exponential map of the unitary group of degree one, $U(1)$, i.e., the mapping from $\phi \in \mathbb{R}$ to $e^{im\phi} \in \mathbb{S}^1$, whose kernel is \mathbb{Z} to ensure m is quantised to be an integer⁷⁹, such that it corresponds to the isomorphism of $U(1) \cong \mathbb{R}/\mathbb{Z} \cong \mathbb{S}^1$. Consequently, left ($m = 1$) and right ($m = -1$) optical vortices become orthogonal to each other, while the superposition state with certain amplitudes and phases is described by $SU(2)$ symmetry and the associated expectation values of OAM^{64–66} are shown on the extended Poincaré sphere of \mathbb{S}^2 . If we utilise both spin and OAM, structured light is known as a vector vortex beam⁶⁷, which is shown on the higher-order Poincaré sphere^{64–78}.

These significant progresses on manipulating structured light enabled researchers to generate photonic skyrmions^{25–38}. Among many experimental systems to observe skyrmions^{12–20,23–38}, photonics is unique in a sense that skyrmions are realised in a free space, where the system is described by non-interacting free bosons. In fact, photonic skyrmions are made as a superposition state among states with different spin and OAM, while these basis states are degenerate in energy with the same wavelength to ensure the coherence. This is a remarkable difference from the original Skyrme model, where a solitary solution with a finite energy emerged from a certain interacting many-body system^{1,3–5}. $SU(6)$ symmetry of our universe was already spontaneously broken^{10,11,80}, such that it is impossible to examine QCD with exact $SU(6)$ symmetry in the vacuum. Similarly, Faddeev and Niemi proposed a model Hamiltonian to stabilise a knot using a classical field⁴², while Dzyaloshinskii-Moriya interaction is considered for magnetic skyrmions^{12–19}. These models are important to discuss the energetically favourable ground states and to stabilise skyrmions as low-energy excitations^{1,3–5,12–19,42}. On the other hand, non-interacting coherent photons from a laser source are employed for structured light to realise photonic skyrmions^{25–38}, and therefore, no energy barrier is expected among various skyrmionic states. Therefore, photonic skyrmions are ideal to investigate the nature of topological structure associated with the symmetry of coherent photons^{25–38}.

The purpose of this work is to explore the topological stability of photonic skyrmions both theoretically and experimentally. Here, we show that coherent photons have $SU(6)$ symmetry with variable spin and OAM. By changing amplitudes and phases for $SU(6)$ basis states, we can continuously transform various skyrmionic states such as Néel ("Hedgehog") and Bloch states^{25–38}. We also show that skyrmions can be continuously transferred to antiskyrmions and *vice versa* through the recently proposed skyrmionic torus³³, which is characterised by expectation values of spin and OAM. The proposed experimental system can be utilised to examine the $SU(6)$ symmetry^{10,11} of coherent photons.

Results and discussion

Experimental realisation of SU(6) transformation

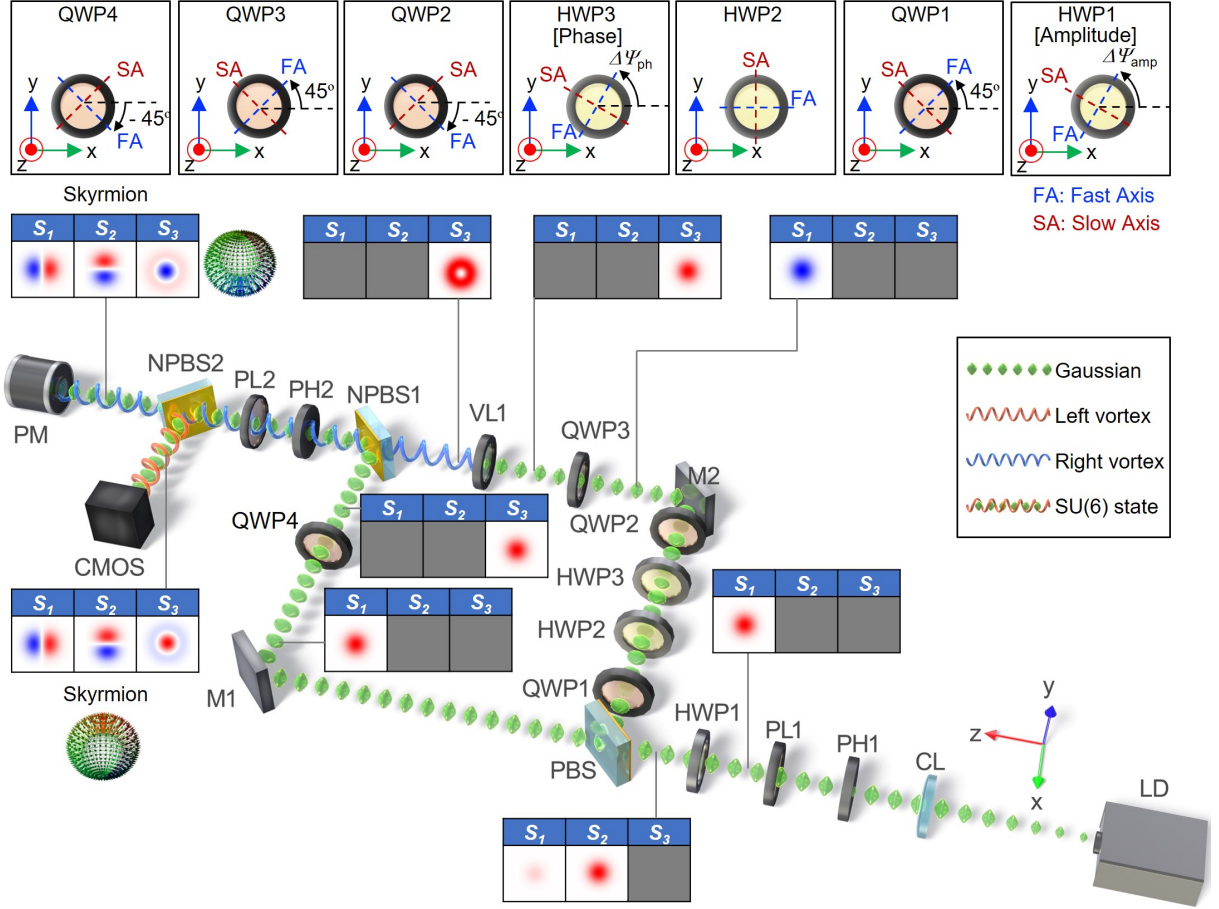


Figure 1. SU(6) transformation for generating skyrmions and antiskyrmions. The input Gaussian beam is set to be the horizontally (H) polarised state of $|H\rangle_S|O\rangle_O$ without an optical vortex. The half-wave-plate1 (HWP1) works as a rotator, whose fast axis (FA) is rotated with the angle $\Delta\Psi_{amp}$ to control amplitudes for horizontal and vertical (V) components under linear polarisation. The beam is split into two paths by the polarisation-beam-splitter (PBS); one path going to quarter-wave-plate1 (QWP1), HWP2, HWP3, and QWP2 is dedicated to control the phase without changing $|V\rangle_S$ by the angle of HWP3, whose FA is rotated with the angle $\Delta\Psi_{ph}$. The beam is then followed by the mirror reflection (M2), polarisation rotation by QWP3, and vortex generation by the vortex lens (VL1) to make the left circularly polarised (\uparrow) right (R) optical vortex, $|\uparrow, R\rangle$ for skyrmions; the other path going to M1 keeps the H-polarisation until QWP4 rotates it to be the left circular polarised (\uparrow) state without a vortex, $|\uparrow, O\rangle$, which is reflected to be $|\downarrow, O\rangle$ at the non-polarisation beam splitter (NPBS). The beam is examined at the polarimeter (PM) for polarisation, and the far-field image is taken at the CMOS camera as a superposition state between $|\uparrow, O\rangle = |3\rangle$ and the right circular polarised left (L) vortex, $|\downarrow, L\rangle = |4\rangle$ for skyrmions. For antiskyrmions, we just need to flip-flop the VL1 to make a superposition state between $|3\rangle$ and $|\downarrow, R\rangle = |5\rangle$ with a right vortex at the camera.

The experimental setup is shown in Fig. 1 (Methods). The primary idea is to realise a generalised Euler's formula,

$$\exp\left(-i\mathcal{J}_j\frac{\delta\phi}{2}\right) = \mathbf{1}\cos\left(\frac{\delta\phi}{2}\right) - i\mathcal{J}_j\sin\left(\frac{\delta\phi}{2}\right), \quad (1)$$

physically in a Mach-Zehnder interferometer⁸¹; we prepare two beams separated at the polarisation-beam-splitter (PBS) with appropriate polarisation controls to change amplitudes, determined by the rotation angle of $\delta\phi/2$; one of the beam is passing through the vortex lens (VL) to generate the beam with OAM, followed by polarisation rotation by the quarter-wave-plate (QWP), corresponding to an $\mathfrak{su}(6)$ operation of \mathcal{J}_j to change both spin and OAM simultaneously; and two beams are

recombined at the non-polarisation-beam-splitter (NPBS). There are wide ranges of polarisation components available in a market, such that it is easier to control polarisation rather than controlling an OAM state directly through a dedicated device. The half-wave-plate (HWP) is equivalent to Pauli matrices of $\hat{\sigma}_1$ and $\hat{\sigma}_2$, depending on the alignment of the fast axis (FA), and the VLs work as ladder operators of $\hat{\lambda}_+^L$ and $\hat{\lambda}_+^R$ to generate left and right optical vortices. It is also worth noting that chiralities for spin and OAM are reversed upon the mirror reflection at NPBS2, such that we need to consider the final output images to realise skyrmions and antiskyrmions at the CMOS camera. The mirror reflection cannot convert a skyrmion to an antiskyrmion, but it reverses the direction for wrapping to represent a spin texture.

Poincaré spheres for skyrmions and antiskyrmions

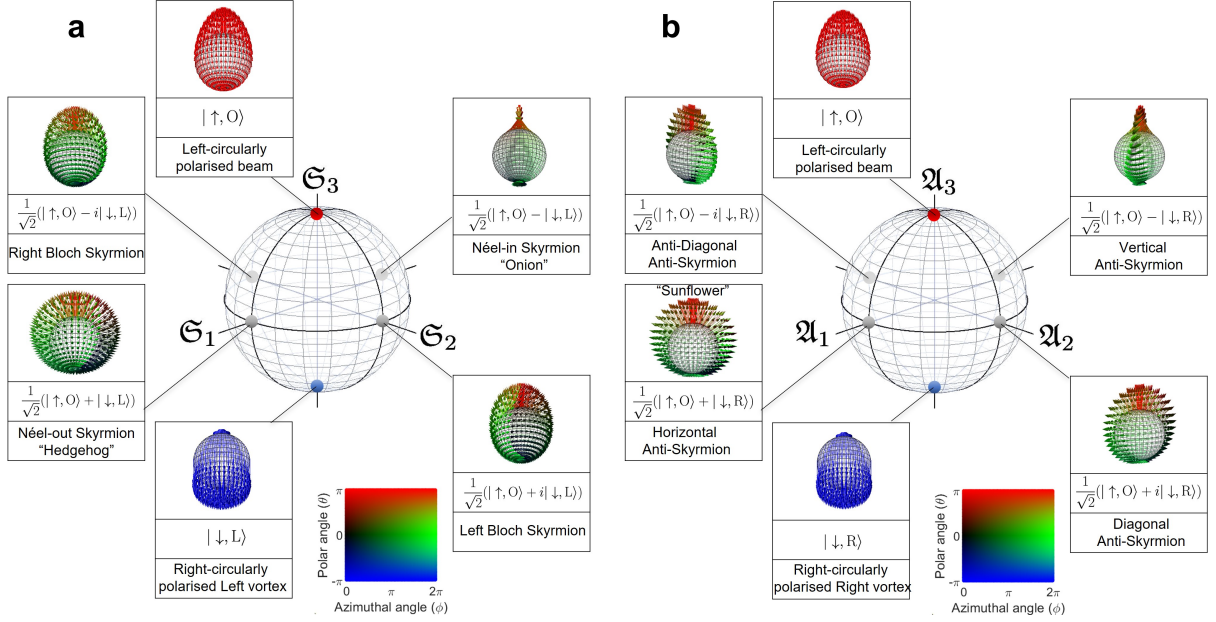


Figure 2. Theoretical expectation for spin textures of photonic skyrmions and antiskyrmions. The radius of the sphere is preserved to be $\hbar N_0$ for arbitrary superposition states, made of two orthogonal states of spin and OAM. **a** Poincaré sphere for skyrmions. ($\mathcal{S}_1, \mathcal{S}_2, \mathcal{S}_3$) are expectation values of $\mathfrak{su}(2)$ generators of rotations to characterise skyrmions. The spin textures are changed upon shifting the phase along the equator, from Néel-out, left Bloch, Néel-in to right Bloch states. **b** Poincaré sphere for antiskyrmions. ($\mathcal{A}_1, \mathcal{A}_2, \mathcal{A}_3$) are expectation values of $\mathfrak{su}(2)$ generators of rotations to characterise antiskyrmions. The spin texture is topologically preserved, while the orientation is changed along the equator.

Theoretical expectations of Poincaré spheres for photonic skyrmions and antiskyrmions^{25–38} are shown in Fig. 2 (Methods). The most famous skyrmion exhibits a staggered spin texture similar to an anti-ferromagnet and thus, named Néel-out skyrmion (Fig. 2a), also known as "Hedgehog", located at $(\mathcal{S}_1, \mathcal{S}_2, \mathcal{S}_3) = \hbar N_0(1, 0, 0)$, whose $SU(6)$ state is given by $|\text{Néel out}\rangle = (|3\rangle + |4\rangle)/\sqrt{2}$. If we rotate the state along the equator, we can realise the Bloch state with the left chirality, $|\text{Left Bloch}\rangle = (|3\rangle + i|4\rangle)/\sqrt{2}$ at $\hbar N_0(0, 1, 0)$, the Néel-in state like an "Onion", $|\text{Néel in}\rangle = (|3\rangle - |4\rangle)/\sqrt{2}$ at $\hbar N_0(-1, 0, 0)$, and the Bloch state with the right chirality, $|\text{Right Bloch}\rangle = (|3\rangle - i|4\rangle)/\sqrt{2}$ at $\hbar N_0(0, -1, 0)$. The north pole is assigned to the purely left-circularly polarised Gaussian beam of $|3\rangle$, and the south pole corresponds to the left OAM state under right-circular polarisation of $|4\rangle$. The states located at the opposite side of the Poincaré sphere are orthogonal to each other, $\langle \text{Néel out} | \text{Néel in} \rangle = \langle \text{Left Bloch} | \text{Right Bloch} \rangle = 0$, because of the orthonormal conditions, $\langle 3 | 3 \rangle = \langle 4 | 4 \rangle = 1$ and $\langle 3 | 4 \rangle = 0$, similar to polarisation states, $\langle H | V \rangle = \langle D | A \rangle = \langle L | R \rangle = 0$.

The antiskyrmions are also shown in Fig. 2b. The horizontal antiskyrmion is described by $|\text{Antiskyrmion}\rangle = (|3\rangle + |5\rangle)/\sqrt{2}$ at $(\mathcal{A}_1, \mathcal{A}_2, \mathcal{A}_3) = \hbar N_0(1, 0, 0)$, which looks like a "Sunflower". Upon changing the phase along the equator, the spin texture of the antiskyrmion is rotated without changing the spin texture. Therefore, they are characterised by the orientation of the spin texture, similar to linearly polarised states. The north pole at $(\mathcal{A}_1, \mathcal{A}_2, \mathcal{A}_3) = \hbar N_0(0, 0, 1)$ is designated for $|3\rangle$, which also corresponds to $(\mathcal{S}_1, \mathcal{S}_2, \mathcal{S}_3) = \hbar N_0(0, 0, 1)$. This implies that there is a path to change continuously from a skyrmion to an antiskyrmion, but this is not clear from these Poincaré spheres. On the other hand, the south pole is assigned for the right vortex, $|5\rangle$ at $(\mathcal{A}_1, \mathcal{A}_2, \mathcal{A}_3) = \hbar N_0(0, 0, -1)$, which is purely polarised to be right-circular polarisation, such that we cannot distinguish the chirality of OAM from the spin textures of $|3\rangle$ and $|4\rangle$.

Phase-shifter operation for skyrmions

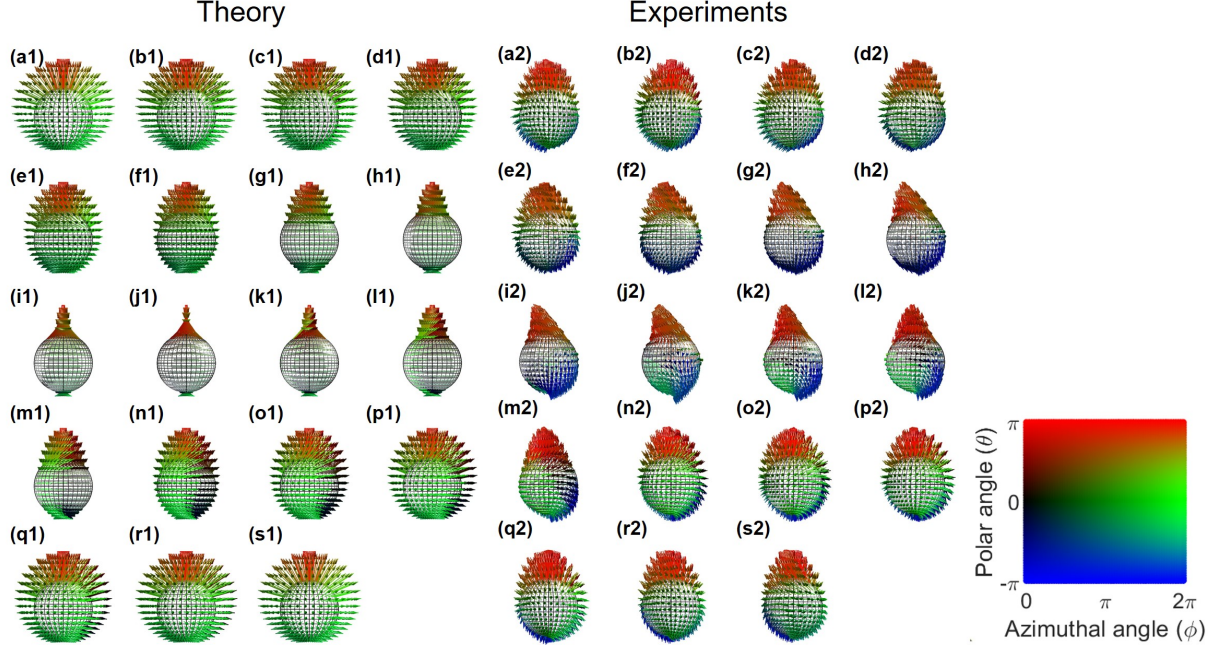


Figure 3. Spin textures of photonic skyrmions upon phase-shifter operations. Skyrmionic states were rotated on the \mathfrak{S}_1 - \mathfrak{S}_2 plane on the Poincaré sphere. (a1)-(s1) theoretical calculations. (a2)-(s2) experiments. The images were shown upon changing the phase by rotating the HWP3 for the angle of $\Delta\Psi_{\text{ph}}$ from 0° to 180° with a step of 10° . (a1) and (a2) Néel-out, "Hedgehog"; (f1) and (f2) right Bloch; (j1) and (j2) Néel-in, "Onion"; (n1) and (n2) left Bloch states, respectively.

We consider rotations over skyrmionic Poincaré sphere of Fig. 2a. It is useful to define an $\text{SU}(2)$ state, given by $(\alpha_3, \alpha_4) = \sqrt{N_0}(e^{-i\phi_s/2} \cos(\theta_s/2), e^{i\phi_s/2} \sin(\theta_s/2)) \in \mathbb{C}^2$, which maps to the point $(\mathfrak{S}_1, \mathfrak{S}_2, \mathfrak{S}_3) = \hbar N_0(\sin \theta_s \cos \phi_s, \sin \theta_s \sin \phi_s, \cos \theta_s) \in \mathbb{S}^2$, such that θ_s and ϕ_s are polar and azimuthal angles, respectively. We show a phase-shifter operator for skyrmions to change the spin texture along the equator of Fig. 2 on the \mathfrak{S}_1 - \mathfrak{S}_2 plane. This was achieved by changing the phase of ϕ_s for the state $(|3\rangle + e^{i\phi_s}|4\rangle)/\sqrt{2}$. In the experiment shown in Fig. 1, the rotation angle of $\Delta\Psi_{\text{ph}}$ of HWP3 induced the phase change as $\phi_s = -2\Delta\Psi_{\text{ph}}$, where the negative sign accounts for the clock-wise rotation in our experiment and the factor of two⁸¹ is coming from the mirror projection of the polarisation state due to the rotated HWP.

Spin textures upon changing the phase are shown in Fig. 3. We used a mapping, named a soup-bubble mapping similar to stereographic mapping, in order to map the local spin distribution taken from a finite far-field image of a closed disk (\mathbb{D}^2) onto a sphere of \mathbb{S}^2 . We confirmed continuous changes from Néel-out (Figs. 3(a1) and 3(a2)), right Bloch (Figs. 3(f1) and 3(f2)), Néel-in (Figs. 3(j1) and 3(j2)) to left Bloch (Figs. 3(n1) and 3(n2)) states both theoretically and experimentally. At each local point in space shown on \mathbb{S}^2 , local spin was rotated for 360° in the clock-wise direction, as expected for the change of $\Delta\Psi_{\text{ph}}$ for 180° . The Néel-out ("Hedgehog", Figs. 3(a1) and 3(a2)) state is characterised by the local spin pointing outwards from the centre, which was continuously changed to be the opposite state of the Néel-in ("Onion", Figs. 3(j1) and 3(j2)) state, whose local spin is pointing inwards to the centre. The left Bloch (Figs. 3(f1) and 3(f2)) state has the spin texture of left circulation seen from the north pole, while the right Bloch (Figs. 3(f1) and 3(f2)) has the opposite chirality of the right circulation on \mathbb{S}^2 .

We have also shown theoretical calculations of local spin profiles (Fig. 4) and corresponding experiments (Fig. 5). They are in reasonable agreement to recognise the topological features, while experimental images were distorted, quantitatively. The main source of the distortions was coming from the precise alignment, required to combine the beams, and we also estimated the deviation of around $\sim 2^\circ$ upon mechanical rotations. Nevertheless, we could confirm the trend that photonic dipole images for S_1 (Figs. 4(a1)-4(s1) and 5(a1)-5(s1)) and S_2 (Figs. 4(a2)-4(s2) and 5(a2)-5(s2)) rotate to the counter-clock-wise direction upon increasing the phase, while images of S_3 (Figs. 4(a3)-4(s3) and 5(a3)-5(s3)) were preserved, because we have not changed the amplitudes among $|3\rangle$ and $|4\rangle$.

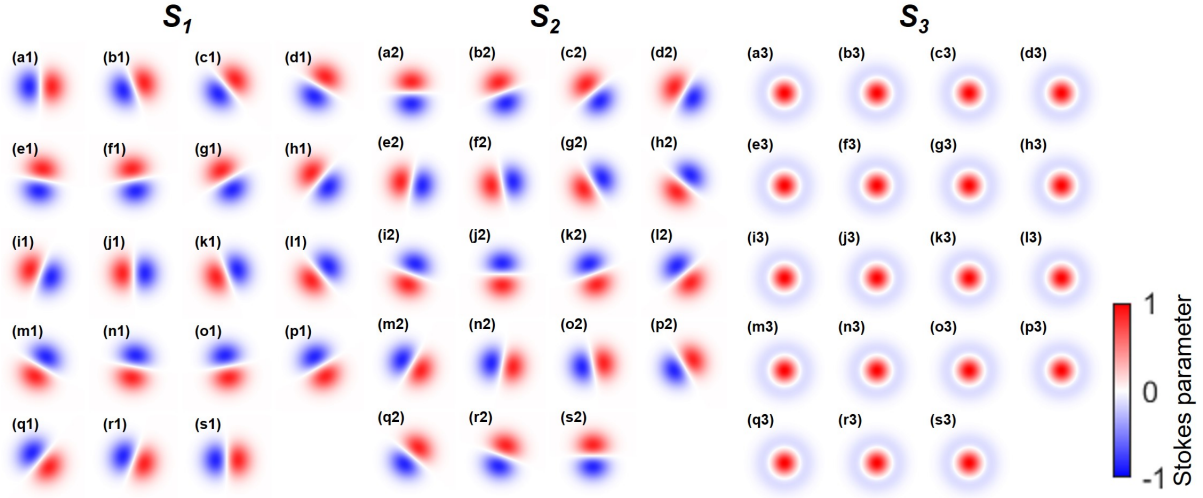


Figure 4. Theoretical local spin profiles for photonic skyrmions upon phase-shifter operations. Calculated Stokes parameters (S_1, S_2, S_3) are shown. The images were calculated for the phase change of ϕ_s from 0° to 360° with a step of 20° . **(a1)-(s1)** S_1 . **(a2)-(s2)** S_2 . **(a3)-(s3)** S_3 . S_1 and S_2 show photonic dipole after projection of polarisation state to horizontal or diagonal directions, respectively, while S_3 is preserved upon changing the phase in the chiral basis.

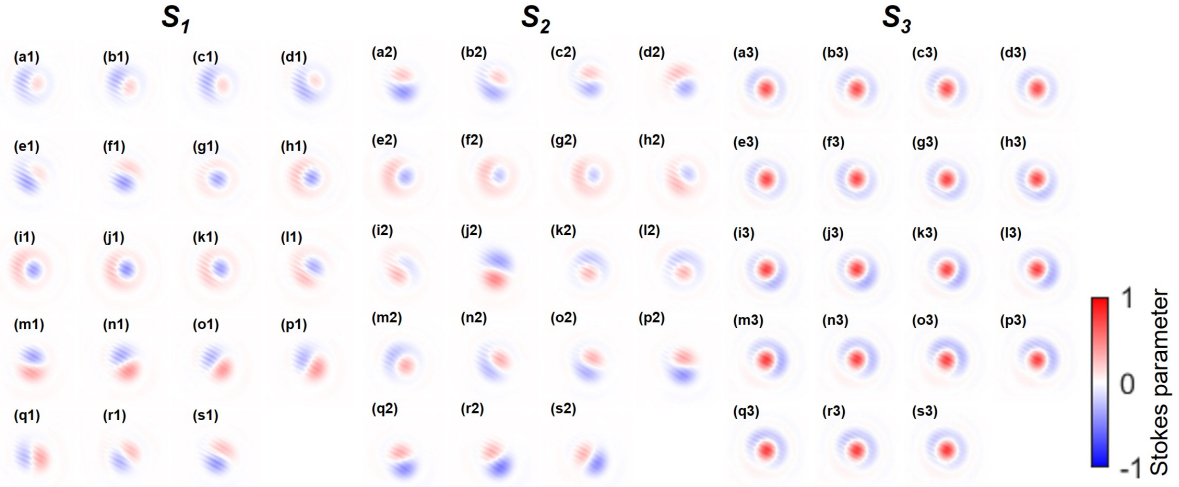


Figure 5. Experimental local spin profiles for photonic skyrmions upon phase-shifter operations. Stokes parameters (S_1, S_2, S_3) measured from far-field images after passing through waveplates and polarisers are shown. The images were shown upon changing the phase by rotating the HWP3 for the angle of $\Delta\Psi_{ph}$ from 0° to 180° with a step of 10° . **(a1)-(s1)** S_1 . **(a2)-(s2)** S_2 . **(a3)-(s3)** S_3 . S_1 and S_2 show rotation of dipoles to the counter-clock-wise direction upon increasing the phase.

Rotator operation for skyrmions

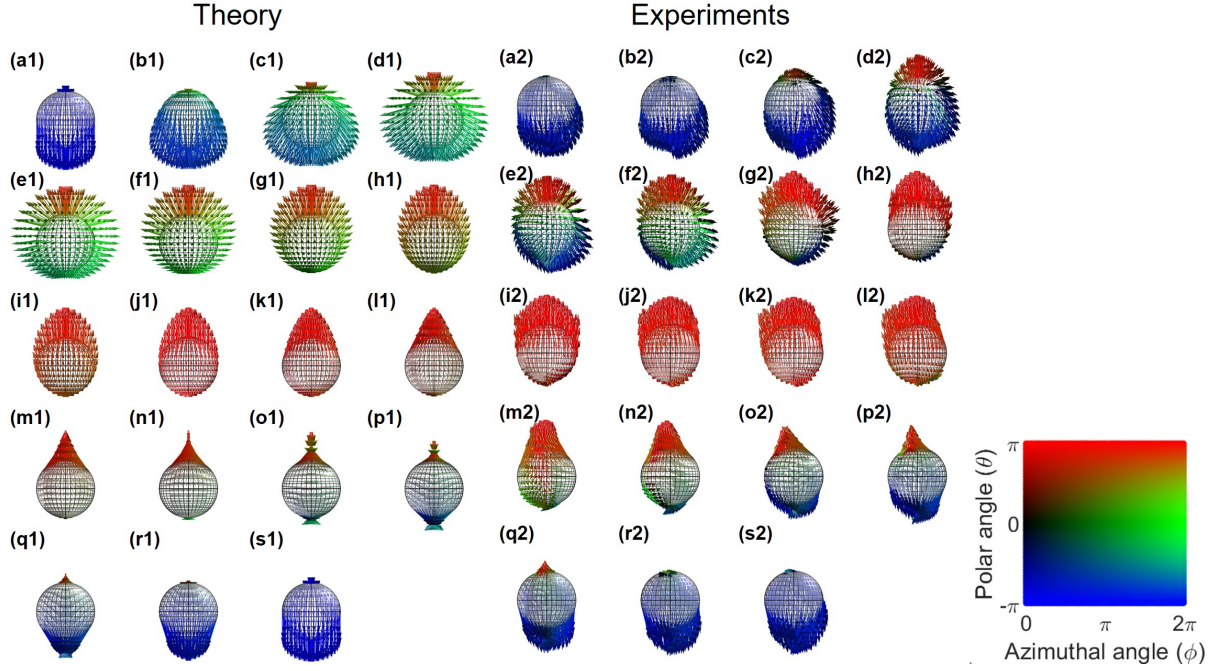


Figure 6. Spin textures of photonic skyrmions upon rotator operations. Skyrmionic states were rotated on the \mathfrak{S}_1 - \mathfrak{S}_3 plane along \mathfrak{S}_2 on the Poincaré sphere. (a1)-(s1) theoretical calculations. (a2)-(s2) experiments. The images were shown upon changing the phase by rotating the HWP1 for the angle of $\Delta\theta_s$ from 0° to 90° with a step of 5° . (a1, a2) Right-circularly-polarised left vortex; (e1, e2) Néel-out; (j1, j2) left-circularly-polarised Gaussian; (o1, o2) Néel-in states, respectively.

Next, we have examined a rotator operation for skyrmions to change the amplitude of θ_s by rotating HWP1 for the amount of $\Delta\Psi_{\text{amp}}$ along the clock-wise direction to give $\theta_s = -4\Delta\Psi_{\text{amp}}$, which is twice compared with that for the phase-shifter, since both horizontal and vertical components were rotated by HPW1, while only the vertical component was affected by HWP3⁸¹. HWP1 allowed to change the splitting ratio to change the amplitudes for $|3\rangle$ and $|4\rangle$. We have adjusted HPW3 to realise the rotation along the \mathfrak{S}_2 to rotate in the \mathfrak{S}_1 - \mathfrak{S}_3 plane (Fig. 6). We confirmed the expected rotation from right-circularly-polarised left vortex (Figs. 6(a1) and 6(a2)), Néel-out (Figs. 6(e1) and 6(e2)), left-circularly-polarised Gaussian (Figs. 6(j1) and 6(j2)) to Néel-in (Figs. 6(o1) and 6(o2)) states.

The local spin profiles are also calculated as shown in Fig. 7, which was experimentally confirmed in Fig. 8. The pure OAM state of $|4\rangle$ has no component on \mathfrak{S}_1 (Fig. 7(a1) and Fig. 8(a1)) and \mathfrak{S}_2 (Fig. 7(a2) and Fig. 8(a2)) due to the right-circular-polarisation (Fig. 7(a3) and Fig. 8(a3)), and it was gradually converted to the Néel-out skyrmion (Figs. 7(e1, e2, e3) and Fig. 8(e1, e2, e3)), followed by the pure Gaussian state with left-circular-polarisation (Figs. 7(j1, j2, j3) and Fig. 8(j1, j2, j3)). We also confirmed that directions of spin components of S_1 and S_2 become opposite to each other between Néel-out (Figs. 7(e1, e2) and Figs. 8(e1, e2)) and Néel-in (Figs. 7(o1, o2) and Figs. 8(o1, o2)) skyrmions. These results prove that we have a continuous path to transform from a standard Gaussian beam without vortex to a photonic skyrmion or *vice versa*. We have also confirmed that various spin textures of skyrmions can be mutually transferred.

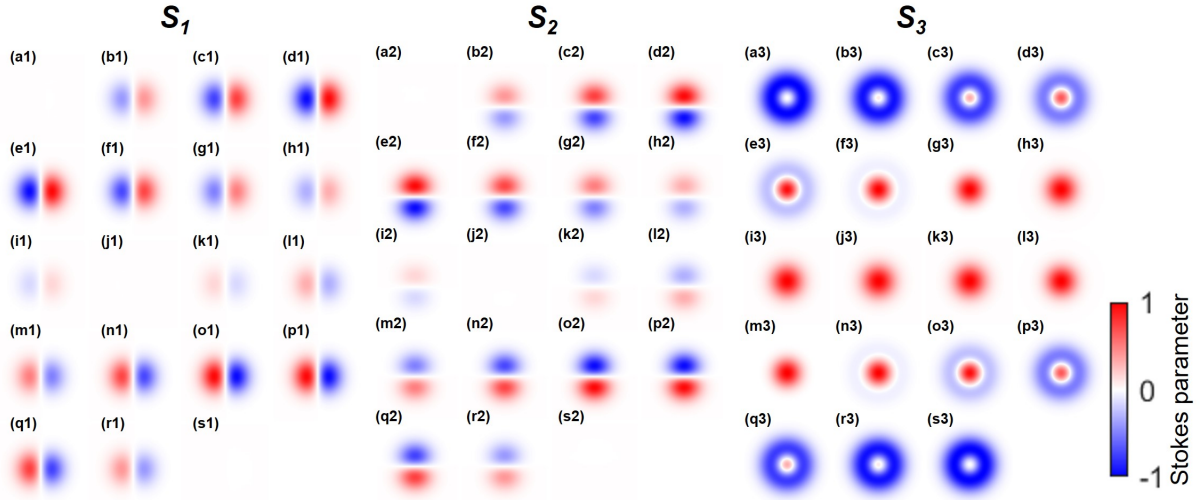


Figure 7. Theoretical local spin profiles for photonic skyrmions upon rotator operations. Calculated Stokes parameters (S_1, S_2, S_3) are shown. The images were calculated for the change in the amplitude given by θ_s from 0° to 360° with a step of 20° . (a1)-(s1) S_1 . (a2)-(s2) S_2 . (a3)-(s3) S_3 . S_1 and S_2 show photonic dipole, if the state is a superposition state between a left vortex and a Gaussian beam, while they disappear, if orbitals are purely made of chiral states at (a1), (a2), (j1), (j2), (s1), and (s2), as is evident in S_3 at (a3), (j3), and (s3), respectively. Néel-out ("Hedgehog") state corresponds to (e1, e2, e3), while the orthogonal state of Néel-in ("Onion") corresponds to (o1, o2, o3), which is characterised by the opposite spin direction in the (S_1, S_2) plane, while S_3 is the same.

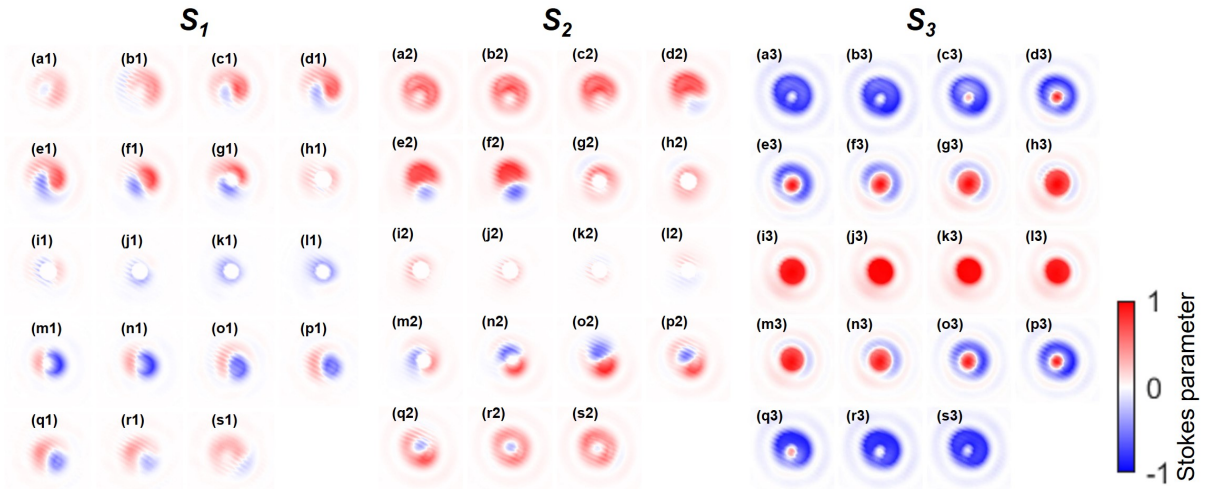


Figure 8. Experimental local spin profiles for photonic skyrmions upon rotator operations. Stokes parameters (S_1, S_2, S_3) measured from far-field images after passing through waveplates and polarisers are shown. The images were shown upon changing the phase by rotating the HWP1 for the angle of $\Delta\Psi_{\text{amp}}$ from 0° to 90° with a step of 5° . (a1)-(s1) S_1 . (a2)-(s2) S_2 . (a3)-(s3) S_3 . The directions of spin become opposite between Néel-out (e1, e2) and Néel-in (o1, o2) states.

Topological transformation from skyrmions to antiskyrmions

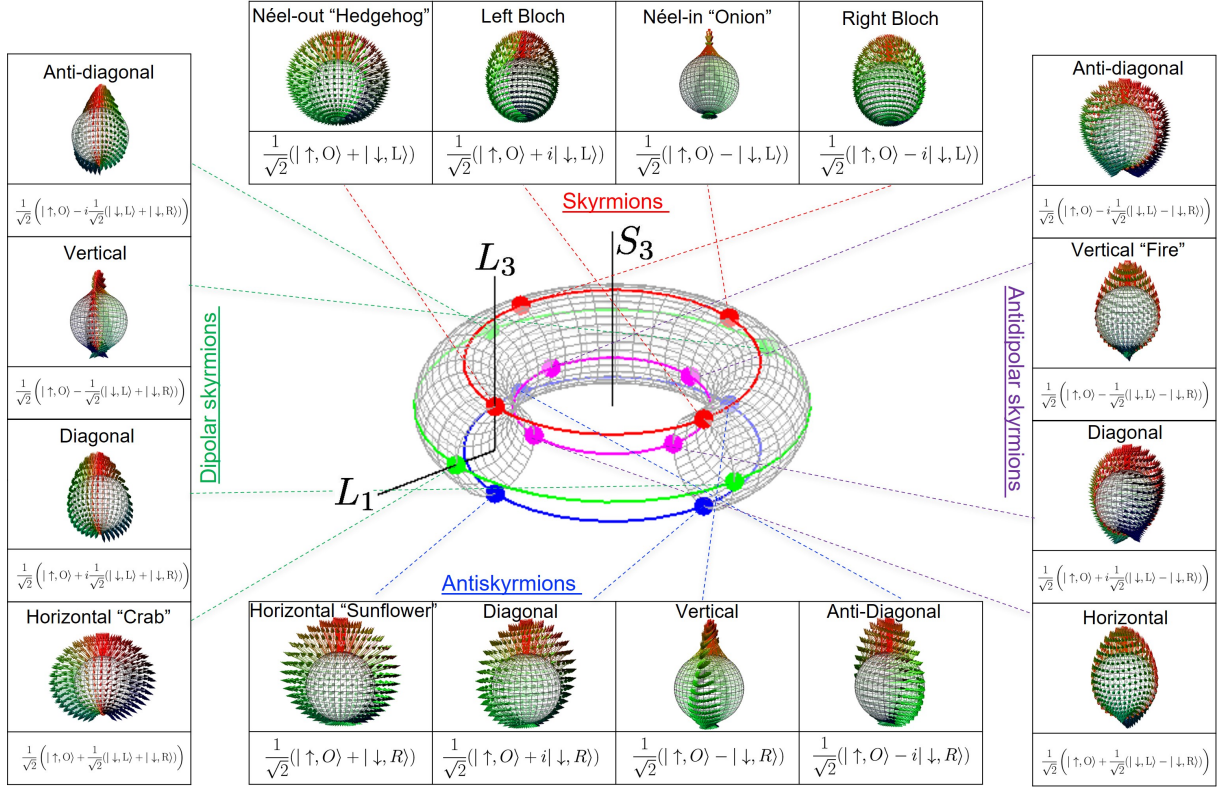


Figure 9. Spin textures on skyrmionic torus \mathbb{T}^2 . An arbitrary skyrmionic state is described as $|\theta_p, \phi_t\rangle = |3\rangle/\sqrt{2} + e^{i\phi_t}(\cos(\theta_p/2)|4\rangle + \sin(\theta_p/2)|5\rangle)/\sqrt{2}$, where θ_p and ϕ_t are poloidal and toroidal angles to determine the point (θ_p, ϕ_t) on the torus. θ_p determines the polar angle on the poloidal circle \mathbb{T}^1 to determine amplitudes for left and right vortices, while ϕ_t determines the azimuthal angle, controlled by the chiral spin angular momentum operator of \hat{S}_3 . Calculated spin textures for typical skyrmions are also shown.

Next, we discuss a continuous unitary transformation from a skyrmion to an antiskyrmion. Above analysis on Poincaré spheres show that a skyrmion is continuously transformed to a pure Gaussian state at the north pole of the skyrmionic \mathbb{S}^2 (Fig. 2a), which also corresponds to the northpole of the antiskyrmionic \mathbb{S}^2 (Fig. 2b), such that it can be continuously transformed to an antiskyrmion. This implies a skyrmion is topologically changed to an antiskyrmion, and in fact, we have a finite overlap between them, as shown by $\langle \text{Néel out} | \text{Antiskyrmion} \rangle = 1/2$. However, the topological connection between them is not clear on Poincaré spheres. Our main interest lies in equators (\mathbb{S}^1) of Poincaré spheres to change spin textures for both skyrmions and antiskyrmions, which allow us to consider a skyrmionic torus of $\mathbb{T}^2 \cong \mathbb{S}^1 \times \mathbb{S}^1$, as proposed by Shen *et al.*³³. According to our consideration on the SU(6) symmetry, we can identify this non-trivial topological feature actually exists in space spanned by spin angular momentum of S_3 together with OAM of (L_1, L_3) , as shown in Fig. 9. Here, we consider a superposition state between a skyrmion and an antiskyrmion, such that the Hilbert space to have at least three orthogonal states are required, which are $|3\rangle$, $|4\rangle$, and $|5\rangle$ in our example shown in Fig. 9, but the other trio ($|1\rangle$, $|2\rangle$, and $|6\rangle$) is also considered by a mirror reflection.

For the skyrmionic torus³³, the state is described by an SU(3) state, $|\theta_p, \phi_t\rangle = |3\rangle/\sqrt{2} + e^{i\phi_t}(\cos(\theta_p/2)|4\rangle + \sin(\theta_p/2)|5\rangle)/\sqrt{2}$, where θ_p is the poloidal angle to change OAM by \hat{L}_2 and ϕ_t is the toroidal angle to change spin by \hat{S}_3 . In addition to standard skyrmions and antiskyrmions, we identify unique spin textures for dipolar and antidipolar skyrmions (Fig. 9). These are coming from photonic dipoles, made by superposition states between left and right vortices^{64–78}. Dipolar skyrmions are made by the superposition states between $|3\rangle$ and the horizontal dipole of $(|4\rangle + |5\rangle)/\sqrt{2}$, with variable phase factor of $e^{i\phi_t}$. The spin texture of the dipolar skyrmion is reminiscent of a "Crab", and their face is rotated upon changing ϕ_t . The skyrmions located at the opposite side along the toroidal direction are orthogonal to each other, similar to polarisation states, such that horizontal and vertical dipolar skyrmions are orthogonal. Similarly, the antidipolar skyrmion is made by the vertical dipole of $(|4\rangle - |5\rangle)/\sqrt{2}$ and $|3\rangle$. The spin texture of the antidipolar skyrmion is reminiscent of a "Fire", which also rotates on ϕ_t .

We can change the rotation along the poloidal direction by using \hat{L}_2 , such that a skyrmion can be continuously changed to

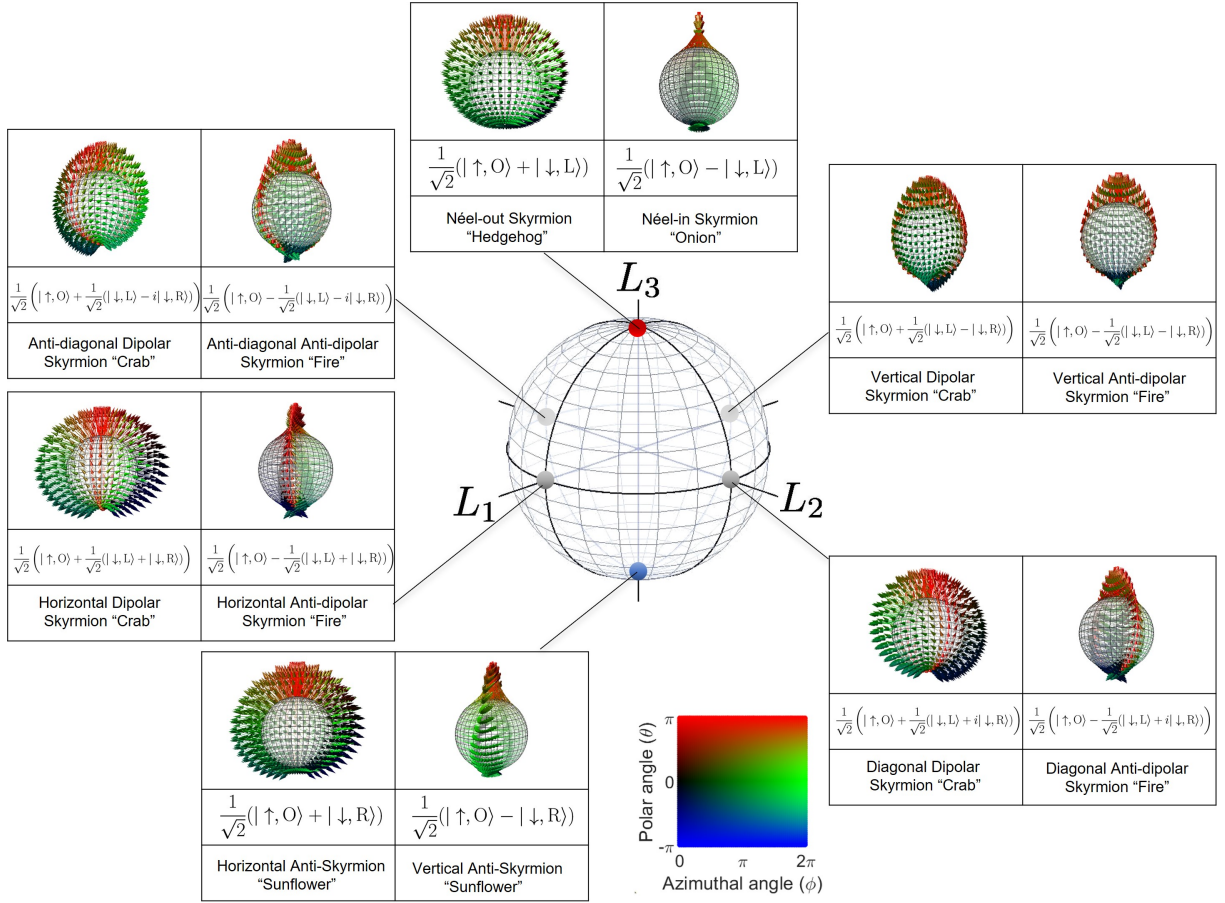


Figure 10. Poincaré sphere of optical angular momentum for various skyrmions. Some skyrmions take the same optical angular momentum, regardless of the orthogonality with different spin textures. For example, the unitary operation to rotate an Néel-out skyrmion along the L_2 axis changes the sing upon one rotation to convert it to a Néel-in skyrmion, which is orthogonal to the Néel-out skyrmion, while both skyrmions give the same expectation values of $(L_1, L_2, L_3) = \hbar N_0/2(0, 0, 1)$.

an antiskyrmion through the path along the troidal direction. The expectation values on the magnitude of OAM determines the radius of the poloidal circle to be $L_p = \sqrt{L_1^2 + L_2^2} = \hbar N_0/2$, where the factor of two was coming from the fact that a standard Gaussian mode of $|3\rangle$ does not carry OAM. It is also noted that states within the poloidal circle under the fixed ϕ_i are not orthogonal to each other, and the amount of the overlap between $|4\rangle$ and $|5\rangle$ can be monitored by the value of L_3 .

These photonic skyrmions are also considered in a Poincaré sphere for OAM, as shown in Fig. 10. Here, it is important to recognise $SU(2)$ is double coverage for $SO(3)$, known as $SU(2) \cong SO(3)/\mathbb{Z}_2$ ^{10,53,56,79}, such that one rotation over the Poincaré sphere changes the phase of the state. This affects our skyrmionic states, and states with different spin textures can give the same expectation values for OAM (Fig. 10). For example, Néel-out and Néel-in skyrmions both give the same expectation values of $(L_1, L_2, L_3) = \hbar N_0/2(0, 0, 1)$, while the spin textures are different. This is unusual to a standard Poincaré sphere to describe polarisation, since two orthogonal states usually occupy different points on the Poincaré sphere. This clearly shows that one Poincaré sphere for OAM is not enough to characterise a skyrmion. The orthogonality of these states were confirmed by our skyrmionic Poincaré sphere (Fig. 2a), such that we need to monitor several order parameters²² to identify the spin textures. For $SU(6)$ states, in general, we found fifteen Poincaré spheres and thirty-five order parameters, which are over-complete to identify a state, composed of \mathbb{C}^6 , which requires only \mathbb{R}^{12} . The skyrmionic torus³³ is one of the best ways to clarify the spin texture of skyrmions. It clearly shows that the topological significance of various skyrmions and we can continuously transform skyrmions on the torus by using the $SU(6)$ transformation.

Outlook towards future applications

Finally, we discuss potential applications of our SU(6) theory for photonic skyrmions. One of the most promising applications would be an optical data storage in silica glass^{82,83}. The advanced laser writing technologies allowed researchers to memorise the variable retardance, depending on the pulse duration and the number of pulses^{82,83}, and the vector vortex beam was successfully observed upon read-out⁸². This means that the local spin texture of photons can be recorded in silica glass, which will be stable for ages⁸³. One can control the chiralities of the spin textures by manipulating the phases and the amplitudes of the laser writing, and the huge Hilbert space of SU(6) would be useful for recording more information in the form of a photonic skyrmion^{25–38} or other spin textures such as photonic Bengal cats to form singlet and triplet states⁸⁴.

Another important application would be fibre optic data transmission for optical communication^{76,85}. Various OAM modes with higher-order topological charges were successfully transmitted and the data transmission as large as 1-Pbps was achieved^{76,85}. We can envisage that we could expand the band width even larger by transmitting photonic skyrmions. However, the effective refractive indices would be different between the fundamental Gaussian mode and the higher-order modes with OAM. The difference induces an effective field for the SU(6) state, which would be described by the generator of $\hat{\lambda}_8$ for OAM. This works as a rotator for OAM, which rotates the azimuthal phase on the skyrmionic or antiskyrmionic Poincaré spheres, depending on the chirality of OAM. The difference of the refractive indices also induces the delay of the OAM mode against the fundamental Gaussian mode, which effectively splits a skyrmion into two pulses. Obviously, this will not be ideal for long-haul optical communication, but it might be useful to analyse a photonic skyrmion to identify the OAM state similar to the polarimetry for polarisation states. Silicon photonic platform will be expected to allow large-scale photonic integrated circuits to generate and detect photonic skyrmions^{30,38}.

Conclusions

We have explored a close relationship between SU(6) symmetry of coherent photons and photonic skyrmions^{25–38}. We have shown coherent photons have SU(6) symmetry for spin and orbital angular momentum both theoretically and experimentally, and found $\mathfrak{su}(2)$ Lie algebra for skyrmions and antiskyrmions. The expectation values of the generators of rotation are shown on Poincaré sphere to characterise various skyrmions with unique spin textures upon changing amplitudes and phases by our experimental set-up, named Poincaré rotator⁸¹. This allows us to consider continuous deformation from a skyrmion to an antiskyrmion by unitary transformation, which was described by a skyrmionic torus³³. The existence of the path to exchange a skyrmion to an antiskyrmion means they are not topologically stable, if there exists an effective field to allow the helical distribution of the local refractive indices. The standard graded-indexed or step-index fibres have no such helical distribution, such that the exchange would be unlikely to be observed upon the fibre transmission. On the other hand, if we intentionally apply appropriate SU(6) operations using Poincaré rotator, it is possible to transform a skyrmion to an antiskyrmion. We believe a photonic skyrmion serves as a valuable platform to examine various theoretical concepts such as topological structure of coherent photons and associated symmetries in a simple bench-top experiment.

Methods

SU(6) symmetry of coherent photons

A single photon with spin ($\sigma = \uparrow, \downarrow$) and OAM (m) is described by a state, $|\sigma, m\rangle = |\sigma\rangle_S \otimes |m\rangle_O = |\sigma\rangle_S |m\rangle_O$, given by a direct product of states for spin, $|\sigma\rangle_S$, and OAM, $|m\rangle_O$. The total state of $|\sigma, m\rangle$ is characterised by a nonseparability^{33,77,86–88} of spin and OAM, which means that we cannot consider an OAM state without spin or *vice versa*. Consequently, states must be orthogonal to each other, if one of spin or OAM is orthogonal, which can be conveniently represented by the Bose-Einstein commutation relationships^{10,11,53}, $[\hat{a}_{\sigma,m}, \hat{a}_{\sigma',m'}^\dagger] = \delta_{m,m'} \delta_{\sigma,\sigma'}$ and $[\hat{a}_{\sigma,m}, \hat{a}_{\sigma',m'}] = [\hat{a}_{\sigma,m}^\dagger, \hat{a}_{\sigma',m'}^\dagger] = 0$, where $\hat{a}_{\sigma,m}^\dagger$ and $\hat{a}_{\sigma,m}$ are creation and annihilation operators for a photon and δ is the Kronecker delta. We consider an arbitrary polarisation state, given by SU(2) symmetry^{57–59,61}, while OAM states are limited to be $m = 0, \pm 1$ for a standard Gaussian mode without a vortex (O), together with left (L) and right (R) twisted states, whose superposition states are represented by SU(3) symmetry^{7–10,79}. Therefore, we have six orthogonal states, represented by SU(6) symmetry^{10,11,79}, and we label the basis state by an integer, $i = (\sigma, m) \in \{1, \dots, 6\}$. In principle, we can extend OAM to have an arbitrary value of $N \in \mathbb{Z}$, using SU(N) symmetry, but we restrict our experimental system to have only three modes for OAM, while we consider an arbitrary superposition state among these six states. After relabelling summarised in Table 1, the commutation relationship is simplified to be $[\hat{a}_i, \hat{a}_j^\dagger] = \delta_{i,j}$.

Table 1. SU(6) states with spin (σ) and orbital angular momentum (OAM), labelled by $i = 1, \dots, 6$. Spin up (\uparrow) and down (\downarrow) correspond to left and right circularly polarised states. For OAM, we consider left (L) and right (R) twisted states with topological charges of $m = \pm 1$ and a Gaussian state (O) without an optical vortex.

| State i | Spin σ | OAM m |
|-------------------------------------|------------------|------------|
| $ 1\rangle = \uparrow, L\rangle$ | 1 | 1 |
| $ 2\rangle = \uparrow, R\rangle$ | 1 | -1 |
| $ 3\rangle = \uparrow, O\rangle$ | 1 | 0 |
| $ 4\rangle = \downarrow, L\rangle$ | -1 | 1 |
| $ 5\rangle = \downarrow, R\rangle$ | -1 | -1 |
| $ 6\rangle = \downarrow, O\rangle$ | -1 | 0 |

We consider generators of rotations to realise superposition among these six orthogonal states, which are known for $\mathfrak{su}(6)$ Lie algebra^{7–10,79}. We need to consider 6×6 matrices, which can be represented by thirty-five generators of rotations (\hat{a}_n ($n = 1, \dots, 35$)), while one degree of freedom disappeared due to the traceless condition, corresponding to the determinant of unity for SU(6) Lie group^{7–10,79}. Three of them are given by $\hat{\sigma} \otimes \hat{\mathbf{1}}$ for spin, using Pauli matrices of $\hat{\sigma} = (\hat{\sigma}_1, \hat{\sigma}_2, \hat{\sigma}_3)$ and the identity operator of $\hat{\mathbf{1}}$, while eight generators of rotations for OAM are given by $\hat{\mathbf{1}} \otimes \hat{\lambda}$, where $\hat{\lambda} = (\hat{\lambda}_1, \dots, \hat{\lambda}_8)$ is Gell-Mann matrices for $\mathfrak{su}(3)$ Lie algebra^{7–10,79}. These generators of rotations will rotate spin and OAM independently, while the rest of generators $\hat{\sigma} \otimes \hat{\lambda}$ will rotate them simultaneously^{7–10,79}. Overall, we have $3 \oplus 8 \oplus 24 = 35$ generators of rotations to cover the $\mathfrak{su}(6)$ Lie algebra^{7–10,79}. The commutation relationship is given by $[\hat{a}_l, \hat{a}_m] = 2i \sum_n g_{lmn} \hat{a}_n$ for $l, m, n = 1, \dots, 35$, using the structure constant^{89,90} of $g_{lmn} = -i \text{tr} [[\hat{a}_l, \hat{a}_m] \hat{a}_n] / 4$. The factor of two is included in front of g_{lmn} in the commutation relationship to compensate for the difference in angles between the Hilbert space and angular momentum space. For example, horizontal and vertical polarisation states are orthogonal for complex electric fields with the angle of 90° , while they are located at the opposite side of the Poincaré sphere with the angle of 180° .

For many-body states, generalised angular momentum operators are defined by

$$\hat{A}_n = \hbar \sum_{i,j=1}^6 \hat{a}_i^\dagger (\hat{a}_n)_{ij} \hat{a}_j, \quad (2)$$

for $n = 1, \dots, 35$, and an SU(6) coherent state is given by

$$|\alpha_1, \alpha_2, \alpha_3, \alpha_4, \alpha_5, \alpha_6\rangle = \prod_{i=1}^6 e^{-\frac{|\alpha_i|^2}{2}} e^{\hat{a}_i^\dagger \alpha_i} |0\rangle, \quad (3)$$

where $\boldsymbol{\alpha} = (\alpha_1, \alpha_2, \alpha_3, \alpha_4, \alpha_5, \alpha_6) \in \mathbb{C}^6$ stands for the SU(6) state. Generalised angular momentum, $\mathbf{A} = (A_1, \dots, A_{35})$, is an expectation value, obtained by

$$A_n = \langle \hat{A}_n \rangle = \hbar \boldsymbol{\alpha}^* \hat{\mathbf{a}}_n \boldsymbol{\alpha}, \quad (4)$$

as if it is an expectation value for a single photon. This is coming from the Bose-Einstein condensation nature of coherent photons to occupy a single quantum state described by α ^{59,81,86,91,92}.

Generalised angular momentum operators are generators of rotation in this SU(6) Hilbert space. This can be confirmed by the exponential map from $\mathfrak{su}(6)$ Lie algebra to SU(6) Lie group by the unitary transformation along the l -th axis

$$\hat{D}_l(\delta\phi) = \exp\left(-\frac{i}{\hbar}\hat{A}_l\frac{\delta\phi}{2}\right), \quad (5)$$

which preserves the form of the coherent state^{59,81}, while the SU(6) state is transferred to be

$$\alpha' = \hat{\mathcal{D}}_l(\delta\phi)\alpha, \quad (6)$$

where α is transposed to be a column vector, and the SU(6) operator is given by the exponential map,

$$\hat{\mathcal{D}}_l(\delta\phi) = \exp\left(-i\hat{a}_l\frac{\delta\phi}{2}\right). \quad (7)$$

The generalised angular momentum after this unitary transformation is given by the quantum-classical correspondence⁸¹,

$$A'_m = \sum_{n=1}^{35} \left(e^{\hat{G}_l\delta\phi}\right)_{mn} A_n, \quad (8)$$

between the change in the SU(N) wavefunction and its expectation value as the SO($N^2 - 1$) angular momentum, where \hat{G}_l is the adjoint operator, whose matrix element is given by the structure constant of g_{lmn} as $(\hat{G}_l)_{mn} = -g_{lmn}$, which satisfies the commutation relationship of $[\hat{G}_l, \hat{G}_m] = \sum_{n=1}^{35} g_{lmn}\hat{G}_n$. This means that the generalised angular momentum is rotated on the hypersphere of \mathbb{S}^{35} by the special orthogonal group of the degree thirty-five, SO(35). In fact, we could prove⁸¹ that the norm is conserved upon the rotation, and the radius of the hypersphere becomes $A_0 = \hbar N_0 \sqrt{5/3}$.

More generally, the rotational axis could be pointing to an arbitrary direction of $\hat{\mathbf{n}} = (n_1, \dots, n_{35})$ in SO(35) space, whose unitary transformation becomes

$$\hat{D}_{\hat{\mathbf{n}}}(\delta\phi) = \exp\left(-\frac{i}{\hbar}\hat{\mathbf{A}} \cdot \hat{\mathbf{n}}\frac{\delta\phi}{2}\right), \quad (9)$$

where $\hat{\mathbf{A}} = (\hat{A}_1, \dots, \hat{A}_{35})$. Lie algebra is vector space^{7-10,79}, such that the vectorial sum rule is applicable and $\hat{\mathbf{A}} \cdot \hat{\mathbf{n}}$ also works as a generator of rotation. It is a straightforward calculation using the Campbell-Baker-Hausdorff formula to confirm the hyperspherical relationship⁸¹

$$\mathbf{A}' = \left(e^{\hat{\mathbf{G}} \cdot \hat{\mathbf{n}}\delta\phi}\right)\mathbf{A}, \quad (10)$$

where the standard matrix product calculus should be applied using the transpose of \mathbf{A} , and $\hat{\mathbf{G}} = (\hat{G}_1, \dots, \hat{G}_{35})$ is angular momentum operator in the adjoint representation. This formula is applicable to an arbitrary value of N for an SU(N) state⁸⁴.

$\mathfrak{su}(2)$ subalgebra for skyrmions and antiskyrmions

We consider a map from an SU(6) state, described by \mathbb{C}^6 , to associated expectation values of generalised angular momentum on \mathbb{S}^{35} . In general, we can realise an arbitrary superposition state with varying amplitudes and phases among six orthogonal states. If we focus on mixing of two orthogonal states, they are described by the $\mathfrak{su}(2)$ subalgebra, whose expectation values are represented on an Poincaré sphere of \mathbb{S}^2 . We have $6 \cdot 5/2 = 15$ ways of selecting two states among six states, such that we can envisage fifteen Poincaré spheres. Three of them are standard Poincaré spheres on polarisation for each pure OAM state (superposition states between $|1\rangle$ and $|4\rangle$, $|2\rangle$ and $|5\rangle$, or, $|3\rangle$ and $|6\rangle$); six of them are Poincaré spheres for OAM under fixed polarisation ($|1\rangle$ and $|2\rangle$, $|1\rangle$ and $|3\rangle$, $|2\rangle$ and $|3\rangle$, $|4\rangle$ and $|5\rangle$, $|4\rangle$ and $|6\rangle$, or, $|5\rangle$ and $|6\rangle$); two of them are singlet-triplet ($|2\rangle$ and $|4\rangle$) and triplet-triplet coupling ($|1\rangle$ and $|5\rangle$). We have already examined these Poincaré spheres previously to confirm the symmetry and a classical entanglement^{59,71,75-78,81,86,93-96}. The rest of four Poincaré spheres are appropriate to examine the coupling among optical modes with and without OAM while chirality of spin is opposite to observe skyrmions ($|3\rangle$ and $|4\rangle$, or, $|2\rangle$ and $|6\rangle$) and antiskyrmions ($|3\rangle$ and $|5\rangle$, or, $|1\rangle$ and $|6\rangle$). Among these four combinations, the combination between $|3\rangle$ and $|4\rangle$ ($|3\rangle$ and $|5\rangle$) and $|2\rangle$ and $|6\rangle$ ($|1\rangle$ and $|6\rangle$) are just mirror symmetric both for spin and OAM upon reflection, and here, we just focus only on the combination of $|3\rangle$ and $|4\rangle$ ($|3\rangle$ and $|5\rangle$) for skyrmions (antiskyrmions).

Lie algebra is vector space, such that we can define another generators of rotation by summing up $\mathfrak{su}(6)$ generators with appropriate factors to change the axis for rotation. For skyrmions, it is useful to define skyrmionic generators of rotation

$$\hat{\mathcal{S}}_1 = \frac{1}{2}(\sigma_1 \otimes \lambda_4 + \sigma_2 \otimes \lambda_5) = \hat{\mathbf{b}}_{13} \quad (11)$$

$$\hat{\mathcal{S}}_2 = \frac{1}{2}(-\sigma_1 \otimes \lambda_5 + \sigma_2 \otimes \lambda_4) = \hat{\mathbf{b}}_{14} \quad (12)$$

$$\hat{\mathcal{S}}_3 = \sigma_3 \otimes \left(\frac{1}{3}\mathbf{1} + \frac{1}{4}\lambda_3 - \frac{\sqrt{3}}{12}\lambda_8 \right) - \mathbf{1} \otimes \left(\frac{1}{4}\lambda_3 + \frac{\sqrt{3}}{4}\lambda_8 \right) = -\frac{\sqrt{3}}{3}\hat{\mathbf{b}}_8 + \frac{\sqrt{6}}{3}\hat{\mathbf{b}}_{15}, \quad (13)$$

which work similarly to Pauli matrices of $(\hat{\sigma}_1, \hat{\sigma}_2, \hat{\sigma}_3)$ for $|3\rangle$ and $|4\rangle$ states for $\mathfrak{su}(2)$ subalgebra, and $\hat{\mathbf{b}}_i$ ($i = 1, \dots, 35$) is a generator of rotation for $\mathfrak{su}(6)$ algebra in a Cartan-Dynkin formalism¹⁰. Similarly, for antiskyrmions, we define antiskyrmionic generators of rotation

$$\hat{\mathcal{A}}_1 = \frac{1}{2}(\sigma_1 \otimes \lambda_6 + \sigma_2 \otimes \lambda_7) = \hat{\mathbf{b}}_{20} \quad (14)$$

$$\hat{\mathcal{A}}_2 = \frac{1}{2}(-\sigma_1 \otimes \lambda_7 + \sigma_2 \otimes \lambda_6) = \hat{\mathbf{b}}_{21} \quad (15)$$

$$\hat{\mathcal{A}}_3 = \sigma_3 \otimes \left(\frac{1}{3}\mathbf{1} - \frac{1}{4}\lambda_3 - \frac{\sqrt{3}}{12}\lambda_8 \right) + \mathbf{1} \otimes \left(\frac{1}{4}\lambda_3 - \frac{\sqrt{3}}{4}\lambda_8 \right) = -\frac{\sqrt{3}}{3}\hat{\mathbf{b}}_8 + \frac{\sqrt{6}}{12}\hat{\mathbf{b}}_{15} + \frac{\sqrt{10}}{4}\hat{\mathbf{b}}_{24} \quad (16)$$

to define another $\mathfrak{su}(2)$ subalgebra, describing for the coupling between $|3\rangle$ and $|5\rangle$. They are described by 2×2 Pauli matrices for the Hilbert space, spanned by $|3\rangle$ and $|4\rangle$ ($|3\rangle$ and $|5\rangle$), for skyrmions and antiskyrmions, respectively. For many-body coherent states, we define skyrmionic and antiskyrmionic $\text{SU}(2)$ generators of rotation

$$\hat{\mathcal{S}}_j = \hbar \begin{pmatrix} \hat{a}_3^\dagger & \hat{a}_4^\dagger \end{pmatrix} \hat{\mathcal{S}}_j \begin{pmatrix} \hat{a}_3 \\ \hat{a}_4 \end{pmatrix} \quad (17)$$

$$\hat{\mathcal{A}}_j = \hbar \begin{pmatrix} \hat{a}_3^\dagger & \hat{a}_5^\dagger \end{pmatrix} \hat{\mathcal{A}}_j \begin{pmatrix} \hat{a}_3 \\ \hat{a}_5 \end{pmatrix}, \quad (18)$$

for $j = 1, 2, 3$, whose expectation values are $(\langle \mathcal{S}_1 \rangle, \langle \mathcal{S}_2 \rangle, \langle \mathcal{S}_3 \rangle)$ and $(\langle \mathcal{A}_1 \rangle, \langle \mathcal{A}_2 \rangle, \langle \mathcal{A}_3 \rangle)$, respectively. The operators $\hat{\mathcal{S}}_j$ and $\hat{\mathcal{A}}_j$ are made of $\mathfrak{su}(6)$ operators, but they are essentially equivalent to $\mathfrak{su}(2)$ operators for skyrmions and antiskyrmions, respectively, such that we can utilise generalised Euler's formulas

$$\exp\left(-i\hat{\mathcal{S}}_j \frac{\delta\phi}{2}\right) = \mathbf{1} \cos\left(\frac{\delta\phi}{2}\right) - i\hat{\mathcal{S}}_j \sin\left(\frac{\delta\phi}{2}\right) \quad (19)$$

$$\exp\left(-i\hat{\mathcal{A}}_j \frac{\delta\phi}{2}\right) = \mathbf{1} \cos\left(\frac{\delta\phi}{2}\right) - i\hat{\mathcal{A}}_j \sin\left(\frac{\delta\phi}{2}\right), \quad (20)$$

which are continuous transformations from the identity operator of $\mathbf{1}$.

Experimental setup

Our experimental setup of a Pincaré rotator is shown in Fig. 1. We used a Laser Diode (LD), which was operated under constant current of 220mA at the wavelength was 532 nm. The beam shape was adjusted by a collimator lens (CL) with the focal length of 100mm, followed by a pin hole (PH0) with the diameter of 200 μm . We used standard optical components to control polarisation such as a polariser (PL), a half-wave-plate (HWP), a quarter-wave-plate (QWP), a polarisation-beam-splitter (PBS), a mirror (M), a non-polarisation-beam-splitter (NPBS), a polarimeter (PM), and a complementary-metal-oxide-semiconductor camera (CMOS). Here, we have mechanically rotated HWP1 to change amplitudes before PBS, while the series of operations by QSP1, HWP2, HWP3, and QWP2 were employed to control the phase, whose amount was controlled by the rotation angle of HWP3. QWP3 and QWP4 were used to rotate the polarisation state to be left or right circularly polarised state. The polarisation state was checked by a PM with optional PL2. The final image was taken by CMOS with and without PL2. We took far-field images for six polarisation states of $|L\rangle$, $|R\rangle$, $|H\rangle$, $|V\rangle$, $|D\rangle$, and $|A\rangle$ using waveplates and polarisers to observe the spin texture.

References

1. Skyrme, T. H. R. A non-linear field theory. *Proc. Roy. Soc. Lond.* **260**, 127–138 (1961). DOI 10.1098/rspa.1961.0018.
2. Skyrme, T. H. R. A unified field theory of mesons and baryons. *Nucl. Phys.* **31**, 556–569 (1962). DOI 10.1016/0029-5582(62)90775-7.
3. Witten, E. Baryons in the $1/N$ expansion. *Nucl. Phys. B* **160**, 57–115 (1979). DOI 10.1016/0550-3213(79)90232-3.
4. Adkins, G. S., Nappi, C. R. & Witten, E. Static properties of nucleons in the Skyrme model. *Nucl. Phys. B* **228**, 552–566 (1983). DOI 10.1016/0550-3213(83)90559-X.
5. D'Hoker, E. & Farhi, E. Skyrmions and/in the weak interactions. *Nucl. Phys. B* **241**, 109–28 (1984). DOI 10.1016/0550-3213(84)90200-1.
6. 't Hooft, G. A planar diagram theory for strong interactions. *Nucl. Phys. B* **72**, 461–473 (1974). DOI 10.1016/0550-3213(74)90154-0.
7. Gell-Mann, M. The eightfold way: A theory of strong interaction symmetry. *U.S. Dep. Energy, Off. Sci. Tech. Inf.* (1961). URL <https://www.osti.gov/biblio/4008239>. DOI 10.2172/4008239.
8. Ne'eman, Y. Derivation of strong interactions from a gauge invariance. *Nuc. Phys.* **26**, 222–229 (1961). DOI 10.1016/0029-5582(61)90134-1.
9. Gell-Mann, M. A schematic model of baryons and mesons. *Phys. Lett.* **8**, 214–215 (1964). DOI 10.1016/S0031-9163(64)92001-3.
10. Georgi, H. *Lie Algebras in Particle Physics: from Isospin to Unified Theories (Frontiers in Physics)* (Westview Press, Massachusetts, 1999).
11. Weinberg, S. *The Quantum Theory of Fields: Foundations volume 1* (Cambridge University Press, Cambridge, 2005).
12. Döring, W. Point singularities in micromagnetism. *J. Appl. Phys.* **39**, 1006–1007 (1968). DOI 10.1063/1.1656144.
13. Belavin, A. A. & Polyakov, A. M. Metastable states of two-dimensional isotropic ferromagnets. *JETP Lett.* **22**, 245–247 (1975). URL https://jetpletters.ru/ps/1529/article_23383.shtml.
14. Bogdanov, A. & Hubert, A. Thermodynamically stable magnetic vortex states in magnetic crystals. *J. Magn. Magn. Mater.* **138**, 255–269 (1994). DOI 10.1016/0304-8853(94)90046-9.
15. Mühlbauer, S. *et al.* Skyrmion lattice in a chiral magnet. *Science* **323**, 915–919 (2009). DOI 10.1126/science.1166767.
16. Tonomura, A. *et al.* Real-space observation of skyrmion lattice in helimagnet MnSi thin samples. *Nano Lett.* **12**, 1673–1677 (1986). DOI 10.1021/nl300073m.
17. Nagaosa, N. & Tokura, Y. Topological properties and dynamics of magnetic skyrmions. *Nat. Nanotechnol.* **8**, 899–911 (2013). DOI 10.1038/NNANO.2013.243.
18. Han, J. H. *Skyrmions in Condensed Matter* (Springer, Charm, Switzerland, 2017).
19. Göbel, B., Mertig, I. & Tretiakov, O. A. Beyond skyrmions: Review and perspectives of alternative magnetic quasiparticles. *Phys. Rep.* **895**, 1–28 (2021). DOI 10.1016/j.physrep.2020.10.001.
20. Ezawa, Z. F. *Quantum Hall Effects: recent theoretical and experimental developments* (World Scientific, 2013).
21. Rybakov, F. N., Garaud, J. & Babaev, E. Stable Hopf-Skyrme topological excitations in the superconducting state. *Phys. Rev. B* **100**, 094515 (2019). DOI 10.1103/PhysRevB.100.094515.
22. Zhang, S. C. A unified theory based on $SO(5)$ symmetry of superconductivity and antiferromagnetism. *Science* (1997). DOI 10.1126/science.275.5303.1089.
23. Ackerman, P. J. & Smalyukh, I. I. Diversity of knot solitons in liquid crystals manifested by linking of preimages in torons and hopfions. *Phys. Rev. X* **7**, 011006 (2017). DOI 10.1103/PhysRevX.7.011006.
24. Ho, T. L. Spinor Bose condensates in optical traps. *Phys. Rev. Lett.* **81**, 742 (1998). DOI 10.1103/PhysRevX.7.011006.
25. Ranãda, A. F. A topological theory of the electromagnetic field. *Lett. Math. Phys.* **18**, 97–106 (1989). DOI 10.1007/BF00401864.
26. Beckley, A. M., Brown, T. G. & Alonso, M. A. Full Poincaré beams. *Opt. Exp.* **10**, 10777–10785 (2010). DOI 10.1364/OE.18.010777.
27. Beckley, A. M., Brown, T. G. & Alonso, M. A. Full Poincaré beams II: partial polarization. *Opt. Exp.* **12**, 9357–9362 (2012). DOI 10.1364/OE.20.009357.

28. Tsesses, S. *et al.* Optical skyrmion lattice in evanescent electromagnetic fields. *Science* **361**, 993–996 (2018). DOI 10.1126/science.aau0227.
29. Gao, S., Speirits, F. C., Castellucci, F., Franke Arnold, S. & Banett, S. M. Paraial skyrmionic beams. *Phys. Rev. A* **102**, 053513 (2000). DOI 10.1103/PhysRevA.102.053513.
30. Lin, W., Ota, Y., Arakawa, Y. & Iwamoto, S. Microcavity-based generation of full Poincaré beams with arbitrary skyrmion numbers. *Phys. Rev. Res.* **3**, 023055 (2021). DOI 10.1364/OPTICA.540469.
31. Lei, X. *et al.* Photonic spin lattices: Symmetry constraints for skyrmion and meron topologies. *Phys. Rev. Lett.* **127**, 237403 (2021). DOI 10.1103/PhysRevLett.127.237403.
32. Zhu, J., Liu, S., Zhang, Y. S., Li, C. F. & Guo, G. C. Synthesis and observation of optical skyrmionic structure in free space. *Phys. Rev. A* **110**, 043522 (2024). DOI 10.1103/PhysRevA.110.043522.
33. Shen, Y., Martínez, E. C. & Rosales-Guzmán, C. Generation of optical skyrmions with tunable topological textures. *ACS Photon.* **9**, 296–303 (2022). DOI 10.1021/acsphotonics.1c01703.
34. Parmee, C. D., Dennis, M. R. & Ruostekoski, J. Optical excitations of skyrmions, knotted solitons, and defects in atoms. *Commun. Phys.* **5**, 54 (2022). DOI 10.1038/s42005-022-00829-y.
35. McWilliam, A. *et al.* Topological approach of characterizing optical skyrmions and multi-skyrmions. *Laser Photonics Rev.* **17**, 2300155 (2023). DOI 10.1002/lpor.202300155.
36. Shen, Y. *et al.* Optical skyrmions and other topological quasiparticles of light. *Nat. Photon.* **18**, 15–25 (2023). DOI 10.1038/s41566-023-01325-7.
37. Cisowski, C., Ross, C. & Franke-Arnold, S. Building paraxial optical skyrmions using rational maps. *Adv. Photonics Res.* **4**, 2200350 (2023). DOI 10.1002/adpr.202200350.
38. Lin, W., Ota, Y., Arakawa, Y. & Iwamoto, S. On-chip optical skyrmionic beam generators. *Optica* **11**, 1588–1594 (2024). DOI 10.1364/OPTICA.540469.
39. Piette, B. M. A. G., Schroers, B. J. & Zakrzewski, W. J. Dynamics of baby skyrmions. *Nuc. Phys. B* **439**, 205–235 (1995). DOI 10.1016/0550-3213(95)00011-G.
40. Penrose, R. & Rindler, W. *Spinors and Space-Time: Volume I, Two-Spinor Calculus and Relativistic Fields* (Cambridge University Press, Cambridge, 1984).
41. Gladikowski, J. & Hellmund, M. Static solitons with nonzero Hopf number. *Phys. Rev. D* **56**, 5194–5199 (1997). DOI 10.1103/PhysRevD.56.5194.
42. Faddeev, L. & Niemi, A. J. Stable knot-like structures in classical field theory. *Nature* **387**, 58–61 (1997). DOI 10.1038/387058a0.
43. Chen, B. G., Ackerman, P. J., Alexander, G. P., Kamien, R. D. & Smalyukh, I. I. Generating the hopf fibration experimentally in nematic liquid crystals. *Phys. Rev. Lett.* **110**, 237801 (2013). DOI 10.1103/PhysRevLett.110.237801.
44. Kobayashi, M. & Nitta, M. Torus knots as Hopfions. *Phys. Lett. B* **728**, 314–318 (2014). DOI 10.1016/j.physletb.2013.12.002.
45. Sugic, D. *et al.* Particle-like topologies in light. *Nat. Commun.* **12**, 6785 (2021). DOI 10.1038/s41467-021-26171-5.
46. Ehrmanntraut, D. *et al.* Optical second-order skyrmionic hopfion. *Optica* **10**, 725–731 (2023). DOI 10.1364/OPTICA.487989.
47. Wan, C., Shen, Y., Chong, A. & Zhan, Q. Scalar optical hopfions. *eLight* **2**, 22 (2022). DOI 10.1186/s43593-022-00030-2.
48. Wang, H. & Fan, S. Photonic spin hopfions and monopole loops. *Phys. Rev. Lett.* **131**, 263801 (2023). DOI 10.1103/PhysRevLett.131.263801.
49. Shen, Y. *et al.* Topological transformation and free-space transport of photonic hopfions. *Adv. Photonics* **5**, 15001 (2023). DOI 10.1117/1.AP.5.1.015001.
50. Rybakov, F. N. *et al.* Magnetic hopfions in solids. *APL Mater.* **10**, 111113 (2022). DOI 10.1063/5.0099942.
51. Hopf, H. Über die abbildungen der dreidimensionalen sphäre auf die kugelfläche. *Math. Ann.* **104**, 637–665 (1931). DOI 10.1007/BF01457962.
52. Urbantke, H. Two-level quantum systems: States, phases, and holonomy. *Am. J. Phys.* **59**, 503 (1991). DOI 10.1119/1.16809.

53. Sakurai, J. J. & Napolitano, J. J. *Modern Quantum Mechanics* (Cambridge University Press, Cambridge, 2020).
54. Caldeira, A. O. & Leggett, A. J. Influence of dissipation on quantum tunneling in macroscopic systems. *Phys. Rev. Lett.* **46**, 211 (1981). DOI 10.1103/PhysRevLett.46.211.
55. Leggett, A. J. & Garg, A. Quantum mechanics versus macroscopic realism: is the flux there when nobody looks? *Phys. Rev. Lett.* **54**, 857 (1985). DOI 10.1103/PhysRevLett.54.857.
56. Nakahara, M. *Geometry, Topology and Physics* (Taylor and Francis Group, Boca Raton, 2003).
57. Stokes, G. G. On the composition and resolution of streams of polarized light from different sources. *Trans. Camb. Phil. Soc.* **9**, 399–416 (1851). DOI 10.1017/CBO9780511702266.010.
58. Poincaré, J. H. *Théorie mathématique de la lumière* (G. Carré, 1892).
59. Glauber, R. J. Coherent and incoherent states of the radiation field. *Phys. Rev.* **131**, 2766 (1963). DOI 10.1103/PhysRev.131.2766.
60. Nielsen, M. & Chuang, I. *Quantum Computation and Quantum Information* (Cambridge Univ. Press, Cambridge, 2000).
61. Born, M. & Wolf, E. *Principles of Optics* (Cambridge University Press, Cambridge, 1999).
62. Couillet, P., Gil, L. & Rocca, F. Optical vortices. *Opt. Commun.* **73**, 403–408 (1989). DOI 10.1016/0030-4018(89)90180-6.
63. Allen, L., Beijersbergen, M. W., Spreeuw, R. J. C. & Woerdman, J. P. Orbital angular momentum of light and the transformation of Laguerre-Gaussian laser modes. *Phys. Rev. A* **45**, 8185–8189 (1992). DOI 10.1103/PhysRevA.45.8185.
64. Padgett, M. J. & Courtial, J. Poincaré-sphere equivalent for light beams containing orbital angular momentum. *Opt. Lett.* **24**, 430–432 (1999). DOI 10.1364/OL.24.000430.
65. Milione, G., Sztul, H. I., Nolan, D. A. & Alfano, R. R. Higher-order poincaré sphere, stokes parameters, and the angular momentum of light. *Phys. Rev. Lett.* **107**, 053601 (2011). DOI 10.1103/PhysRevLett.107.053601.
66. Naidoo, D. *et al.* Controlled generation of higher-order poincaré sphere beams from a laser. *Nat. Photon.* **10**, 327–332 (2016). DOI 10.1038/NPHOTON.2016.37.
67. Rosales-Guzmán, C., Ndagano, B. & Forbes, A. A review of complex vector light fields and their applications. *J. Opt.* **20**, 123001 (2018). DOI 10.1088/2040-8986/aaeb7d.
68. Forbes, A. & Nape, I. Quantum mechanics with patterns of light: Progress in high dimensional and multidimensional entanglement with structured light. *Avs Quantum Sci.* **1**, 011701 (2019). DOI 10.1116/1.5112027.
69. Shen, Y. *et al.* Optical vortices 30 years on: OAM manipulation from topological charge to multiple singularities. *Light. Sci. Appl.* **8**, 90 (2019). DOI 10.1038/s41377-019-0194-2.
70. Shen, Y., Wang, Z., Fu, X., Naidoo, D. & Forbes, A. SU(2) Poincaré sphere: A generalised representation for multidimensional structured light. *Phys. Rev. A* **102**, 031501(R) (2020). DOI 10.1103/PhysRevA.102.031501.
71. Shen, Y. Rays, waves, SU(2) symmetry and geometry: toolkits for structured light. *J. Opt.* **23**, 124004 (2021). DOI 10.1088/2040-8986/ac3676.
72. Angelsky, O. V. *et al.* Structured light control and diagnostics using optical crystals. *Front. Phys.* **9**, 715045 (2021). DOI 10.3389/fphy.2021.715045.
73. Yang, L. P. & Jacob, Z. Non-classical photonic spin texture of quantum structured light. *Commun. Phys.* **4**, 221 (2021). DOI 10.1038/s42005-021-00726-w.
74. Andrews, D. L. Symmetry and quantum features in optical vortices. *Symmetry* **13**, 1368 (2021). DOI 10.3390/sym.13081368.
75. Forbes, A., d. Oliveira, M. & Dennis, M. R. Structured light. *Nat. Photon.* **15**, 253–262 (2021). DOI 10.1038/s41566-021-00780-4.
76. Ma, M., Lian, Y., Wang, Y. & Lu, Z. Generation, transmission and application of orbital angular momentum in optical fiber: A review. *Front. Phys.* **9**, 773505 (2021). DOI 10.3389/fphy.2021.773505.
77. Shen, Y. & Rosales-Guzmán, C. Nonseparable states of light: From quantum to classical. *Laser Photonics Rev.* **16**, 2100533 (2022). DOI 10.1002/lpor.202100533.
78. Nape, I., Sephton, B., Ornelas, P., Moodley, C. & Forbes, A. Quantum structured light in high dimensions. *APL Photon.* **8**, 051101 (2023). DOI 10.1063/5.0138224.
79. Fulton, W. & Harris, J. *Representation Theory: A First Course* (Springer, New York, 2004).

80. Nambu, Y. Quasi-particles and gauge invariance in the theory of superconductivity. *Phys. Rev.* **117** (1960). DOI 10.1103/PhysRev.117.648.
81. Saito, S. SU(N) symmetry of coherent photons controlled by rotated waveplates. *Heliyon* **10**, e34423 (2024). DOI 10.1016/j.heliyon.2024.e34423.
82. Sakakura, M., Lei, Y., Wang, L., Yu, Y. H. & Kazansky, P. G. Ultralow-loss geometric phase and polarization shaping by ultrafast laser writing in silica glass. *Light. Sci. Appl.* **9**, 15 (2020). DOI 10.1038/s41377-020-0250-y.
83. Wang, H., Lei, Y., Shayeganrad, G., Svirko, Y. & Kazansky, P. G. Increasing efficiency of ultrafast laser writing via nonlocality of light-matter interaction. *Laser Photonics Rev.* **18**, 2301143 (2024). DOI 10.1002/lpor.202301143.
84. Saito, S. Spin textures of coherent photons with SU(4) symmetry. *Results Phys.* **61**, 107745 (2024). DOI 10.1016/j.rinp.2024.107745.
85. Liu, R. *et al.* 1-Pbps orbital angular momentum fibre-optic transmission. *Light. Sci. Appl.* **11**, 202 (2022). DOI 10.1038/s41377-022-00889-3.
86. Spreew, B. J. C. A classical analogy of entanglement. *Found. Phys.* **28**, 361–374 (1998). DOI 10.1023/A:1018703709245.
87. Milione, G., Nguyen, T. A., Leach, J., Nolan, D. A. & Alfano, R. A. Using the nonseparability of vector beams to encode information for optical communication. *Opt. Lett.* **40**, 4887 (2015). DOI 10.1364/OL.40.004887.
88. McLaren, M., Konrad, T. & Forbes, A. Measuring the nonseparability of vector vortex beams. *Phys. Rev. A* **92**, 023833 (2015). DOI 10.1103/PhysRevA.92.023833.
89. Haber, H. E. Useful relations among the generators in the defining and adjoint representations of SU(n). *SciPost Phys. Lect. Notes* **21**, 1–11 (2021). DOI 10.21468/SciPostPhysLectNotes.21.
90. Bossion, D. & Huo, P. General formulas of the structure constants in the $\mathfrak{su}(n)$ Lie algebra. *ArXiv* **2108**, 07219 (2021). DOI 10.48550/arXiv.2108.07219.
91. Jones, R. C. A new calculus for the treatment of optical systems i. description and discussion of the calculus. *J. Opt. Soc. Am.* **31**, 488–493 (1941). DOI 10.1364/JOSA.31.000488.
92. Fano, U. A Stokes-parameter technique for the treatment of polarization in quantum mechanics. *Phys. Rev.* **93**, 121–123 (1954). DOI 10.1103/PhysRev.93.121.
93. Sasada, H. & Okamoto, M. Transverse-mode beam splitter of a light beam and its application to quantum cryptography. *Phys. Rev. A* **168**, 012323 (2003). DOI 10.1103/PhysRevA.68.012323.
94. Rosen, G. F. Q., Tamborenea, P. I. & Kuhn, T. Interplay between optical vortices and condensed matter. *Rev. Mod. Phys.* **94**, 035003 (2022). DOI 10.1103/RevModPhys.94.035003.
95. Cisowski, C., Götze, J. B. & Franke-Arnold, S. *Colloquium*: Geometric phases of light: Insights from fiber bundle theory. *Rev. Mod. Phys.* **94**, 031001 (2022). DOI 10.1103/RevModPhys.94.031001.
96. Lopes, J. H., Soares, W. C., d. L. Bernardo, B., Caetano, D. P. & Canabarro, A. Linear optical CNOT gate with orbital angular momentum and polarisation. *Quantum Inf. Process.* **18**, 256 (2019). DOI 10.1007/s11128-019-2369-4.

Acknowledgements

The author would like to express sincere thanks to Prof I. Tomita for continuous discussions and encouragements. This work is supported by JSPS KAKENHI Grant Number JP 18K19958.

Author contributions statement

The author confirms being the sole contributor of this work and has approved it for publication.

Competing interests

The author declares no conflict of interest.